

all other primer sequences used in this study. For RT-PCR of LOC203547 mRNA in patient lymphoblasts or fibroblasts and of minigene mRNAs following transfection in C2C12 cells, 1 μg total RNA was converted into cDNA using oligo (dT) primers and then PCR-amplified for 20 cycles. For qRT-PCR of these mRNAs, relative standard curves normalized to β -actin were used. The standard curves were prepared from control lymphoblasts or C2C12 cDNA at 1, 10, 10^2 , 10^3 , and 10^4 dilution factors. Individual reactions contained 0.5 μL template cDNA of appropriate concentration for linear amplification based on the standard curve, 100 ng of each primer, and 1xSYBR Green PCR master mix (Applied Biosystems) to a final volume of 20 μL . Reactions were carried out using Applied Biosystems 7900HT for 40 cycles (95 $^{\circ}\text{C}$, 15''; 60 $^{\circ}\text{C}$, 60''). PCR product purity was determined by melting curve analysis. Each cDNA preparation was tested in triplicate. Data were analyzed using SDS2.1 v.2.1.0.3 (Applied Biosystems). Values exceeding two standard deviations were excluded. Construction of the minigenes is described in Supplemental Methods and Supplemental Fig. 5.

V-ATPase assays

Total protein was measured using the Bradford assay and a BSA standard curve. Hydrolysis of ATP by V-ATPase was measured by the bafilomycin A1-sensitive method adapted from Huss et al. [11]. Microsomal pellets were thawed on ice and suspended in ATPase buffer (10 mM HEPES-Tris pH 7, 5 mM MgCl_2 , 50 mM KCl, 10 mM NaN_3 , 1 mM levamisole–10 mM NaF, 0.7 $\mu\text{g}/\text{ml}$ leupeptin, 0.7 $\mu\text{g}/\text{ml}$ pepstatin A, 48.72 $\mu\text{g}/\text{L}$ PMSF) to a protein concentration of 0.75–1.75 mg/ml (see Supplemental methods for subcellular fractionation procedures). The reaction mix contained 1 mM ATP substrate, 3 μg total protein samples, 5 μM valinomycin, 5 μM nigericin, 1 mM orthovanadate, 10 $\mu\text{g}/\text{mL}$ oligomycin in ATPase buffer made to 70 μL final volume and incubated in the presence and absence of 10 nM bafilomycin for 30' at 37 $^{\circ}\text{C}$. ATP hydrolysis was terminated with 13 % SDS and 100 mM EDTA. Control reactions were done to correct any non-enzymatic hydrolysis of ATP or orthophosphate contamination from reagents by adding the stop solution prior to ATP substrate addition. Reaction was initiated by addition of Taussky-Shorr color reagent (0.5 % w/v FeSO_4 , 0.5 % w/v ammonium molybdate, and 0.5 M H_2SO_4) [35]. The reaction was incubated for 20' at RT and inorganic phosphate (P_i) was measured by absorbance at 650 nm. Standard calibration curve was generated using (P_i) standards (0, 2.5, 5, 10, 25, 50, 100, and 150 nmole). Mean values and standard deviation were calculated from three independent assay repeats done in triplicate.

Complementation assay

Saccharomyces cerevisiae BY4742 wild-type strain ($\text{MAT}\alpha$, $\text{his3}\Delta 1$, $\text{leu2}\Delta 0$, $\text{lys2}\Delta 0$, and $\text{ura3}\Delta 0$) and *vma21* Δ mutant (BY4742, $\text{Mat}\alpha$, $\text{his3}\Delta 1$, $\text{leu2}\Delta 0$, $\text{lys2}\Delta 0$, $\text{ura3}\Delta 0$, and YGR105w::kanMX4) were obtained from the European *Saccharomyces Cerevisiae* Archive for Functional Analysis (Euroscarf). LOC203547 was cloned into yeast expression plasmid pCADNS under alcohol dehydrogenase (*ADH*) promoter, terminator, and transformed into strains BY4742 and *vma21* Δ . Transformants were selected on synthetic complete media without leucine and assayed for viability on medium containing 10 mM CaCl_2 , YPD pH 7.5 (alkaline conditions), and ability to grow on glycerol as the sole carbon source.

Determination of lysosomal pH

Lysosomal pH was measured according to Demarex et al. [6]. Fibroblasts were seeded on 25 mm circular glass cover slips and grown to confluence in DMEM with 10 % FBS at 37 $^{\circ}\text{C}$ and 5 % CO_2 . At confluence, cells were washed twice with PBS and serum-starved by adding DMEM containing 2 % FBS for 40 min. Lysosomes were loaded overnight with 0.5 mg/ml dextran-coupled Oregon Green 514 (Molecular Probes) in DMEM supplemented with 10 % FBS, chased for 2 h in DMEM (10 % FBS), and washed to remove residual dextran. Ratiometric fluorescence microscopy was performed using a Leica DMIRB microscope with 100X (1.4 NA) oil objective. Fluorescence images were acquired at excitation wavelengths of 440 ± 10 and 490 ± 10 nm. Image acquisition and analysis were performed using software MetaMorph (Universal Imaging). Regions of interest (ROI), representing late endosomes/lysosomes as resolved by light microscopy, were defined as areas above a certain fluorescence threshold in the 490 nm excitation channel. Mean intensity ratio between 490 and 440 nm excitation channels was calculated for each ROI, and mean ratio weighted by ROI size was then calculated for each imaged fibroblast. Calibration curves were obtained after 4 min equilibration in nigericin (5 μM) containing MES buffers (in mM: 30 NaCl, 130 KCl, 30 MgCl_2 , 25 MES, and 20 glucose) with different pH values adjusted between pH 3.0 and 7.0. Ratios were converted to pH using the calibration curve fitted to a sigmoidal equation. At least six lysosomes within the same cell (at least five cells per sample) were covered, and the experiment was repeated six times for significance.

Long-lived protein degradation

Intracellular protein degradation was measured as described by Cuervo et al. [5]. Confluent cells were labeled with

200 $\mu\text{Ci/ml}$ [^3S]methionine/[^3S]cysteine Redivue in vitro cell labeling mix for 48 h at 37 °C, and washed and maintained in complete medium with excess of unlabeled methionine and leucine. Following this, aliquots of media and cells were taken at different times for 72 h and precipitated in TCA, and proteolysis was measured. Media contained MG-132 to eliminate proteasomal contribution. Total radioactivity incorporated in cellular proteins was determined in triplicate samples as the amount of acid-precipitable radioactivity. Proteolysis was calculated as the % acid-precipitable radioactivity (protein) transformed into acid-soluble radioactivity (amino acids and peptides) at the different analyzed time points. Values were expressed as % protein degraded. In separate sets, the above proteolysis experiments were performed in the presence of 15 mM NH_4Cl and 100 μM leupeptin or 10 mM 3-methyladenine (3MA) in the culture medium during the chase. The former combination effectively blocks all types of autophagy [27] and 3MA blocks macroautophagy [20]. The inhibitory effect on the lysosomal system was calculated as the decrease in protein degradation sensitive to NH_4Cl /leupeptin. Non-lysosomal proteolysis was subtracted from total proteolysis (the former was negligible, <3 %, and unvarying). The inhibitory effect on macroautophagy was determined as the decrease in protein degradation sensitive to NH_4Cl /leupeptin that is also inhibited by 3MA. Non-macroautophagy-dependent degradation was calculated as the % protein degradation sensitive to NH_4Cl /leupeptin that is not inhibited by 3MA.

Knockdown of VMA21 mRNA

pSUPER RNAi system [3] was used for specific downregulation of mouse *Vma21* expression. RNAi expressing sequences (Supplemental Table 1) for targeting the 3'UTR region of *Vma21* were cloned into pSUPER RNAi system. Forward and reverse strands of the oligonucleotides were annealed to form a duplex and were inserted into *Bg*II–*Hind*III cleavage site of the pSUPER RNAi vector prelinearized with restriction enzymes. The recombinant plasmid was transformed into XLBlue *E.coli* strain, and the resultant cells were cultured in LB-ampicillin containing media. Recombinant clones positive for siRNA were selected and used to transfect NIH3T3 cells. Downregulation of *Vma21* was assessed using quantitative RT-PCR and Western blotting. A mock transfection with empty pSUPER vector was used to control any non-specific effects. The transfected cells were examined for phenotypic changes with electron microscopy.

Amino acid starvation, and stimulation with leucine or leucine ester

Amino acid starvation methods were adapted from Zoncu and colleagues [38]. Control and patient fibroblasts grown

in DMEM with 10 % dialysed FCS were rinsed three times with amino acid-free RPMI and incubated in the same for 4 h. After a 4-hour starvation period, cells were stimulated by adding leucine or leucine methyl ester for 20 min (not exceeding a final concentration of 0.05 mM) in RPMI in independent experiments. The cells were lysed using RIPA buffer with protease inhibitor cocktail, and Western blot was performed using anti-phospho p70S6 kinase antibody.

Measurement of total amino acids

The samples for estimation of free amino acid concentration were prepared based on a previously described method [10]. Fibroblasts grown to confluence in DMEM with 10 % FBS were scraped and frozen in 200 μl of phosphate buffered saline at -80 °C for 15 min and thawed at 4 °C followed by 20 °C for one cycle. For the next cycle of freeze–thaw, samples were kept at 4 °C for an hour followed by 6–8 min at 20 °C. For the third freeze thaw cycle, cells were frozen again at -80 °C for 15 min, and thawed 40 min at 4 °C and 8 min at 20 °C. The third cycle was repeated three times. The free amino acid concentration was determined by a colorimetric method ($\lambda = 570$ nm) using the amino acid quantitative kit from Biovision as per the manufacturer's instructions. To generate a standard curve, 0, 2, 4, 6, 8, and 10 μl of L-amino acid standard was added to each well to generate 0, 8, 16, 24, 32, and 40 nmol/well concentration. The final volume was adjusted to 100 μl /well using L-amino acid assay buffer. The reaction mix consisted of 46 μl of amino acid assay buffer, 2 μl amino acid probe, and 2 μl L-amino acid enzyme mix. To measure the concentration in test samples, the standards and the samples were incubated in 50 μl of reaction mix in a total volume of 150 μl made up with the assay buffer and incubated for 30 min at 37 °C. L-amino acid amount (nmol) was calculated from the standard curve based on absorbance at OD 570 and expressed as nmol/number of cells in each well. Additional controls including a protein BSA sample, a mixture of pure amino acids, and a mixture of protein with amino acids were used to check for false positive results.

Mass spectrometric analyses of intracellular leucine

The intracellular leucine concentrations in patient and control fibroblasts were quantified using LC–MS–MS, applying a modification of a previously described method [30]. Fibroblasts grown to confluence were scraped and centrifuged at 3000 rpm for 10 min at 4 °C. Cell pellets were resuspended in 500 μl methanol and subjected to sonication. 75 μl of cell homogenate was transferred into eppendorf tubes, internal standard (L-leucine-d10 5 ng) added and made up to 1 ml with methanol for protein

precipitation. The mixture was vortexed and centrifuged at $15,000\times g$ for 15 min at 4 °C. Supernatants were transferred to new screw cap tubes and dried under nitrogen gas. Dried residues were derivatized with 100 μ l 3 M HCl-butanol at 65 °C for 20 min. The dried butylated samples were reconstituted in 1 ml of 20 % acetonitrile and 0.1 % formic acid, and transferred to a set of borosilicate auto-sampler vials for injection. Both samples and standard curve were analyzed by liquid chromatography-mass spectrometry MS/MS in a API 4000 triple quadrupole mass spectrometry system (Applied Biosystems). Prior to entering the triple quadrupole MS, leucine was separated from isoleucine using a Dionex Acclaim (Thermo Scientific) organic acid column (5 μ m 120 A, 4.0 \times 250 mm; Dionex), and was eluted over 6 min at a flow rate of 450 μ l/min with an Agilent HPLC 1200. The following butylated transitions were employed: for leucine m/z 188.10/86.100 and for leucine-d10 m/z 198.200/86.100. The concentration of L-leucine was measured by running against L-leucine standard curve (0.5–500 ng) spiked with the same amount of internal standard (L-leucine-d10 5 ng). Endogenous leucine concentrations were calculated using the slope and the positive y-intercept of the calibrators by the Analyst 1.5.2 software (Applied Biosystems/MDS SCIEX). The expected ratio of leucine to the IS (leucine-d10) was plotted against the observed peak area ratio of the analyte to IS to extract the slope and intercept.

Statistical analysis

All statistical analysis was performed by 2-tailed Student's *t* test using Microsoft Excel. A *P* value <0.05 were considered significant. Data are expressed as mean \pm SEM or as mean \pm SD as indicated in corresponding legends. All Western blots were repeated three times to validate the results. Where protein levels were compared, the band intensities measured using Image J program are specified in the corresponding figure legends.

Results

Hypomorphic mutations in the LOC203547 gene cause XMEA

We previously mapped the XMEA gene to a 0.58 Mb region of Xq28 containing four known genes and a predicted fifth gene, LOC203547 [23] (Fig. 1a). We sequenced the exons and flanking intronic sequences of all five genes in XMEA patients from 14 families, and found sequence changes only in LOC203547 which in all families segregated with the disease. To confirm that the changes are mutations, we sequenced LOC203547 in over 450

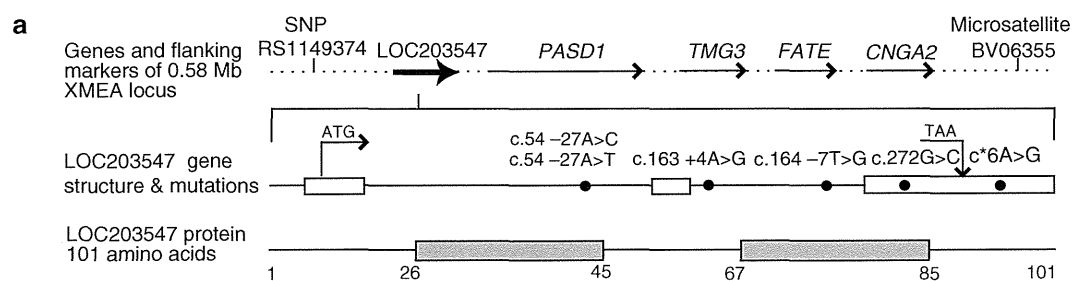
control chromosomes, including 100 from ethnically matched individuals for each mutation, none of which contained the identified changes (Fig. 1b).

LOC203547 has three exons, and a 4.7 Kb transcript expressed ubiquitously (Supplemental Fig. 4a). The mutations consist of six different single-nucleotide substitutions. The first two, c.54–27A>T and c.54–27A>C, eliminate the A nucleotide defining the splice branch point of intron 1. The third, c.163+4A>G, removes the A in the +4 position after exon 2, which contributes to optimal U1 snRNA binding during splicing. The fourth, c.164–7T>G, disrupts the polypyrimidine tract in intron 2, which would reduce the binding efficiency of the U2AF splice factor. The fifth, c.272G>C, is in coding sequence replacing a glycine with alanine, but also abolishes a predicted splice enhancer site. The sixth, c.*6A>G, occurs six nucleotides past the termination codon in the 3'UTR (Fig. 1).

Splice site mutations cause disease by generating abnormal isoforms, or by decreasing mRNA quantity through reduced splicing efficiency. We detected no splice variants by RT-PCR or by Northern blotting (Supplemental Fig. 4B), but a comparison of means of RNA levels by quantitative RT-PCR (qRT-PCR) from patient fibroblasts and lymphoblasts revealed 32–58 % reduction in LOC203547 mRNA, including in patients with the 3'UTR mutation (Fig. 2a, b). Western blots and immunocytochemistry showed that LOC203547 is also reduced at the protein level (Fig. 2c, d). To confirm that these reductions are directly caused by the LOC203547 variants and not secondary disease effects, we generated minigene expression vectors for each splice site change (Supplemental Methods and Supplemental Fig. 5) and transfected them into C2C12 myoblasts. In these experiments, the only difference between each minigene and corresponding wild-type minigene are the single altered LOC203547 nucleotides observed in the patients. qRT-PCR showed >40 % decrease in mRNA from the variant minigenes compared to wild-type (Fig. 2e, f), confirming that the changes cause LOC203547 mRNA downregulation.

LOC203547 is the human ortholog of the yeast V-ATPase assembly chaperone Vma21p

Toward determining whether LOC203547 is the human ortholog of Vma21p we first asked whether its downregulation in XMEA affects the V-ATPase and whether this effect is comparable to the previously characterized effect of Vma21p deficiency in yeast. The yeast *vma21* deletion mutant *vma21* Δ has markedly reduced V-ATPase levels and V-ATPase activity and defective growth. It also exhibits increased free V₁ sector proteins in the cytosol, because V₁ subunits are produced in the cytosol and subsequently added to the V₀ sector assembled in the ER [18].

**b**

Family, ethnicity and number of affected patients per family			Mutation	Relevance, predicted outcome	Controls*	
					T	E
XMEA-1	American	3	c.54 -27A>C	The mutated A nucleotide is the predicted splicing branch point**. The mutation would inhibit nucleophilic attack of the branch point onto the 5' splice site of the first intron during splicing.	360	133
XMEA-2	Italian	1	c.54 -27A>T		360	108
XMEA-3	French	1	c.54 -27A>T	The fourth position after an exon is A in 70% of all exons. This mutation is expected to result in suboptimal binding of the U1 snRNA to the 5' splice site.	360	119
XMEA-4	French	2	c.163 +4A>G		360	119
XMEA-5	French	2	c.163 +4A>G		360	119
XMEA-6	French	2	c.163 +4A>G	This mutation introduces a purine into the polypyrimidine tract of this splice site. This is predicted to decrease the binding strength of the U2AF splice factor.	360	119
XMEA-7	French	4	c.164 -7T>G		465	122
XMEA-8	French	2	c.164 -7T>G		465	122
XMEA-9	French	5	c.164 -7T>G	This coding mutation is predicted to disrupt a binding motif for the SC35 splice factor***. It also changes a glycine to alanine.	465	122
XMEA-10	Finnish	5	c.272G>C		304	84
XMEA-11	Finnish	2	c.272G>C	3' UTR mutation in proximity to the stop codon. This mutation may disrupt binding of transcript stabilization and processing factors.	304	84
XMEA-12	Armenian	7	c.*6A>G		304	92
XMEA-13	American	10	c.*6A>G		304	128
XMEA-14	American	3	c.*6A>G		304	128

Fig. 1 LOC203547 and XMEA mutations. **a** The LOC203547 gene has three exons (*open boxes*). The positions of the six XMEA mutations relative to the LOC203547 exons are depicted by *bullets*. The LOC203547 protein has two predicted transmembrane domains (*grey boxes*). **b** Table of mutations. In the electropherogram panels, *top* is normal sequence and *bottom* sequence is the patient's. * numbers of chromosomes from normal individuals genotyped for

each mutation, T is the total number of chromosomes, E is the number of chromosomes from ethnically matched individuals; ** Prediction by Splicing Sequences Finder—Branch Point Sequence (<http://www.umd.be:2300/searchBP.html>); *** Prediction by Exonic Splicing Enhancer Finder (<http://rulai.cshl.edu/cgi-bin/tools/ESE3/esefinder.cgi?process=home>)

We measured V-ATPase activity in the light membrane fraction (includes all organelles) of XMEA patient lymphoblast extracts and found that it is reduced to 12–22 % of normal (Fig. 3a). In fibroblasts, V-ATPase activity was

reduced to 11–13 % of normal, and in fresh-frozen muscle biopsies to 21–33 % (Fig. 3b). We next assessed the amount of V-ATPases in the light membrane fractions by performing immunoprecipitation and Western blot

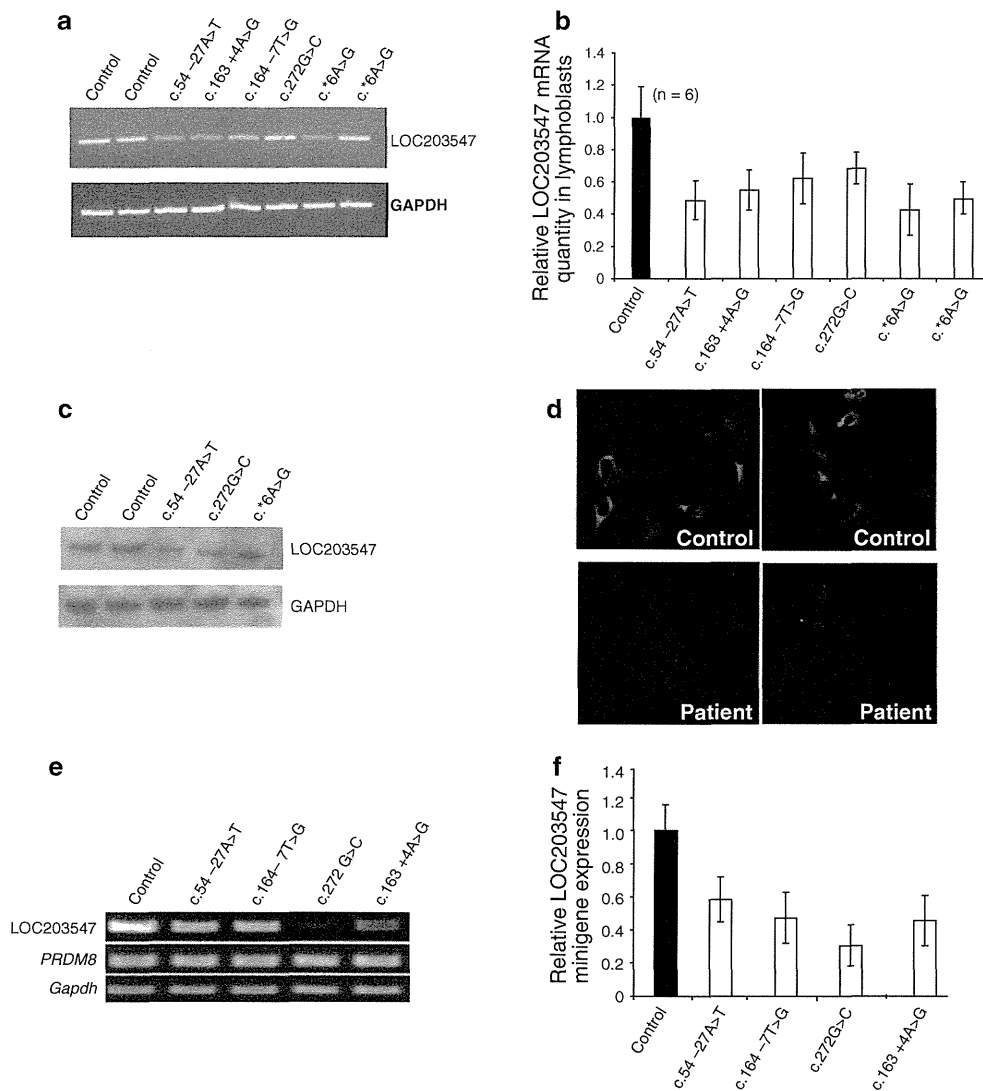
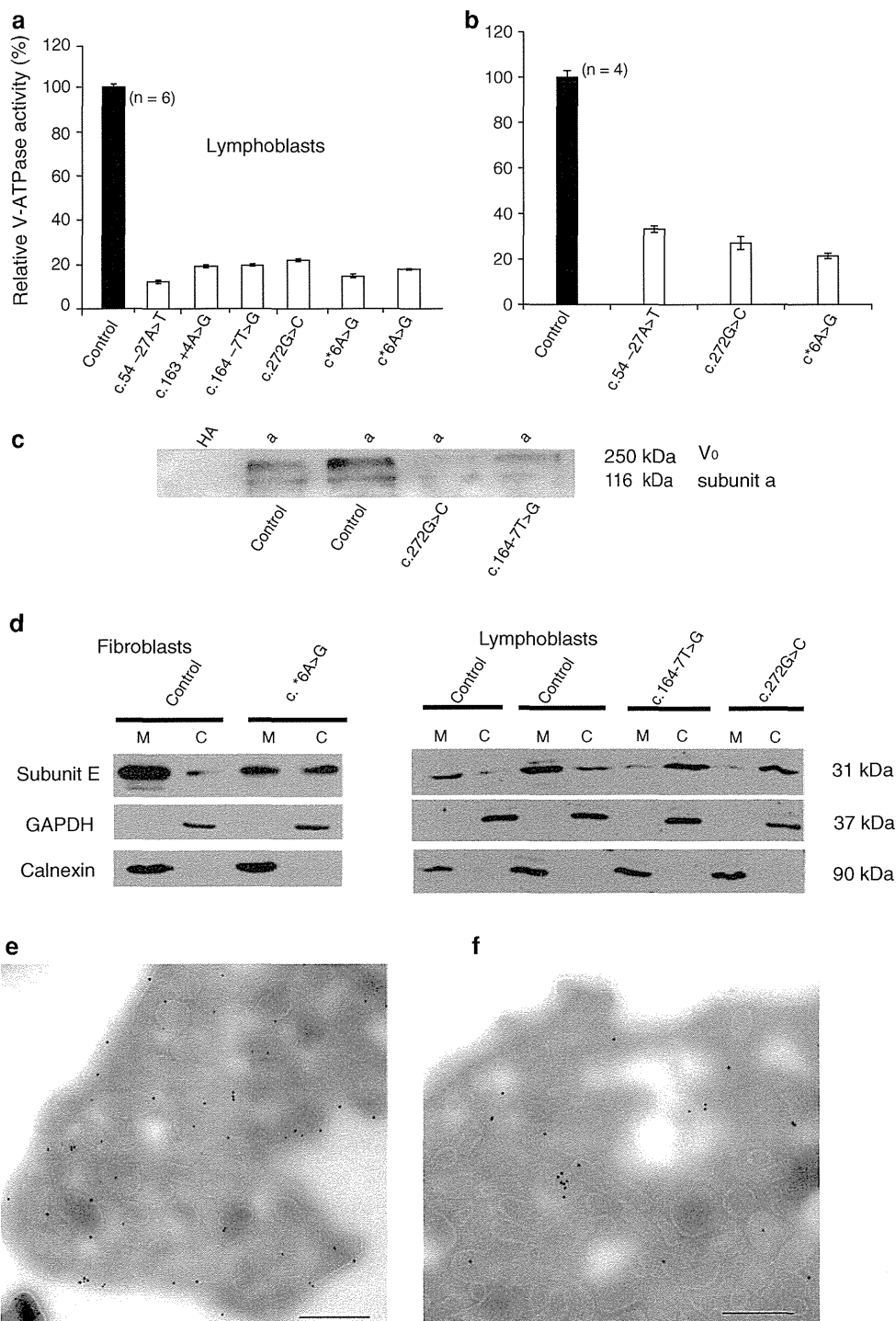


Fig. 2 Effects of XMEA mutations on LOC203547 mRNA and protein. **a** RT-PCR of LOC203547 from patient and control lymphoblast RNA. **b** Quantitative RT-PCR of LOC203547 in lymphoblast RNA measured as a ratio to β -actin. **c** LOC203547 protein in frozen patient and control skeletal muscle by Western blot; mean band intensities were measured using Image J: Control ($n = 2$) 1.19 ± 0.074 ; patient ($n = 3$) 0.46 ± 0.045 . Similar results in fibroblasts shown in Supplemental Fig. 4c. **d** LOC203547 protein in

patient (XMEA-13) and control fibroblasts by immunofluorescence light microscopy. **e** RT-PCR of four LOC203547 minigene constructs following transfection into C2C12 myoblasts, the *PRDM8* gene (in pcDNA 3.1) was cotransfected as transfection efficiency control, endogenous *GAPDH* expression was used as control for cDNA synthesis. **f** Quantitative RT-PCR of above minigenes relative to β -actin. Bars in panels **b** and **f** represent mean \pm standard deviation of three independent experiments

experiments with antibodies against the V-ATPase subunits a and E which showed reduced signal in patients (Fig. 3c, d) indicating that the decreased V-ATPase activity was due to decreased V-ATPase levels which we confirmed by directly counting V-ATPase complexes on intact membranes of intact neutrophils using immunogold electron microscopy (Fig. 3e, f). Western blots of cytosolic and light membrane fractions showed that V_1 subunit E was increased in patient cytosols to an extent similar to its reduction from organellar membranes (Fig. 3d), indicating that the decrease in V-ATPases is due to decreased formation of V_0 complexes. As an assembly chaperone, yeast

Vma21p expectedly interacts with the V_0 complex, and immunoprecipitating it co-precipitates the complex [18]. We show that immunoprecipitating LOC203547 in light membrane fractions of mammalian cells likewise co-precipitates V_0 (Fig. 4a, b), and immunocytochemical experiments show co-localization of LOC203547 with V-ATPase subunits (Supplemental Fig. 6). The contact between yeast Vma21p and V_0 is the V_0 subunit c' [18]. Subunits c' as well as c and c'' are highly homologous proteins that form the yeast V_0 intramembranous rotating cylinder (Supplemental Fig. 1). c' does not exist in mammalian proteomes, and in mammals the V_0 rotating core



utilizes only proteins c and c'' [8]. We, therefore, tested whether LOC203547 interacts with either of these proteins. Immunoprecipitating LOC203547 following full denaturation revealed that subunit c'', but not subunit c, remained bound (Fig. 4c), suggesting that LOC203547 interfaces with the V_0 complex at least in part through c''.

Finally, we asked whether LOC203547 can complement *vma21Δ*. The *vma21Δ* yeast strain is characterized by a well-defined set of growth defects including poor growth on complete media, and the absence of growth on media with nonfermentable carbon sources or with high pH or calcium [18]. We cultured *vma21Δ*, LOC203547-transformed

Fig. 3 Defective V-ATPase activity and assembly in XMEA. **a, b** V-ATPase activity in lymphoblast and skeletal muscle light membrane fractions; *bars* mean \pm standard error of three independent experiments. **c** Immunoprecipitation and Western blotting of lymphoblast light membrane fractions with subunit a antibody, non-denaturing conditions (DTSSP crosslinking and detergent C12E9) used to favor maintaining V_0 assembled. V_0 , which includes subunit a, is 250 kDa in size; subunit a is 116 kDa. In patients, both are reduced (subunit a is known to undergo rapid degradation when unassembled) (2). **d** Western blots of V_1 subunit E in light membrane (Mem) and cytosolic (Cyt) fractions. E is decreased from light membrane fractions and increased in cytosol; band intensities in patients determined using image J software: in fibroblasts from patient c.6*A>G, 0.509 (Mem) and 0.711 (Cyt) vs 1.293 (Mem) and 0.298 (Cyt) in control; in lymphoblasts from patient c.164-7T>G, 0.120 (Mem) and 0.743 (Cyt), and patient c.272G>C, 0.213 (Mem) and 1.251 (Cyt) compared to averages of 0.753 (Mem) and 0.208 (Cyt) in controls. GAPDH and Calnexin used to verify fraction purity. **e, f** Representative EM of neutrophils from normal (**e**) and XMEA (**f**) cells immunogold labeled against subunit a; neutrophils possess large V-ATPase-rich phagosomes, and V-ATPases in the plasma membrane utilized for migration through tissues. In XMEA, gold particle numbers are reduced (*black dots* at the plasma membrane and on the membranes of the phagosomes); *bar*, 0.5 μ m. Actual mean counts from 150 neutrophils from three controls (50 cells per control) and 100 neutrophils from two patients (50 cells/patient) were, in particles/linear μ m: control plasma membrane, 2.7 ± 0.5 , patient plasma membrane, 0.4 ± 0.1 ; control phagosome membrane, 4.3 ± 0.75 , patient phagosome membrane, 1.25 ± 0.06 ; significance <0.001 (student's *t* test)

vma21 Δ , and wild-type yeast for 3 days in YP-glycerol pH 5.5 (glycerol as sole carbon source), YPD pH 7.5 (elevated pH), or YPD pH 5.5 with 10 mM CaCl₂. *Vma21* Δ showed characteristic negligible growth, while LOC203547-transformed *vma21* Δ grew proficiently, and equal to wild-type, on all three media (Fig. 4d), showing that LOC203547 fully rescues *vma21* Δ . Collectively, these results establish that LOC203547 is the human ortholog of Vma21p, and is, hereafter, named VMA21.

The subcellular stations of VMA21 diverge from those of Vma21p

In yeast, Vma21p first interacts in the ER membrane with the V_0 subunit c'. This initiates a stepwise assembly of the other V_0 components, and the presence of Vma21p is necessary throughout the process. Once V_0 is formed, Vma21p accompanies it on COPII vesicles to the Golgi apparatus, where V_1 subunits are added to complete the V-ATPase [18]. Vma21p is retargeted by its carboxy-terminal dilysine signal to the ER, while each V-ATPase is directed to its particular destination based on which isoform of the 'a' subunit was incorporated during V_0 assembly [18]. To determine the subcellular locations in which human VMA21 acts, we stained human fibroblasts (Fig. 5) and C2C12 cells (Supplemental Fig. 7) with VMA21 and organelle-specific antibodies. VMA21

strongly localizes at ER, COPII vesicles, and the ER-Golgi intermediate compartment (ERGIC). It is not present at the Golgi, or beyond (trans-golgi network). VMA21 lacks a dilysine ER return signal consistent with which we find that it has minimal, if any, presence on COPI, the ER return vesicle. There was also no localization on mitochondria and minimal, likely negligible, signal in few peroxisomes and lysosomes (Fig. 5). In summary, the route of VMA21 is diverged from that of its yeast counterpart. It follows the latter's path from ER to ERGIC, but not on to the Golgi, and it does not appear to cycle back to the ER.

Block in the completion of autophagy, associated with upregulation of its initial phases

Autophagy is the degradation of long-lived proteins and other cell components. It is composed of three processes with a common final stage, digestion at low pH by lysosomal hydrolases. In chaperone-mediated autophagy, proteins are taken into lysosomes via receptors. In microautophagy, they are engulfed by lysosomes. In macroautophagy, isolation membranes form in the cytoplasm, surround targeted proteins and other constituents, and fuse with lysosomes. The transitional structures prior to merger with lysosomes are called autophagosomes, and the final organelles autolysosomes. Macroautophagy is the largest contributor to autophagy, and is the process that expands to compensate for insufficiencies in the non-macro autophagic processes, or to meet increased autophagic demands such as during starvation [21].

Based on our finding of decreased V-ATPase activity in XMEA, we predicted that XMEA cells have elevated lysosomal pH and a resultant partial block in the common final degradative stage of autophagy. To test this, we first measured lysosomal pH. We incubated fibroblasts with Oregon green dextran overnight, during which dextran is endocytosed to the lysosome where it fluoresces with an intensity proportional to pH and emits two wavelengths around an isobestic point; fluorescence intensity at one wavelength is inversely proportional to the intensity at the other and their ratio corrects for focal plane artifacts (Supplemental Fig. 8) [26]. pH of patient lysosomes was 0.5 units higher (pH 5.2 vs. 4.7), i.e., three times less $[H^+]$, than that of controls (Fig. 6a). Next, we measured autophagy, by quantifying the degradation of long-lived proteins. We cultured lymphoblasts and fibroblasts for 48 h with radioactive cysteine and methionine. After washing, we chased protein degradation by measuring the TCA soluble fraction of total radioactivity for 72 h. Three types of chase media were used for the calculation of total autophagy, macroautophagy, and non-macro autophagy: routine media, media with lysosomal protease inhibitors (NH₄Cl and leupeptin), and media containing 3-methyl

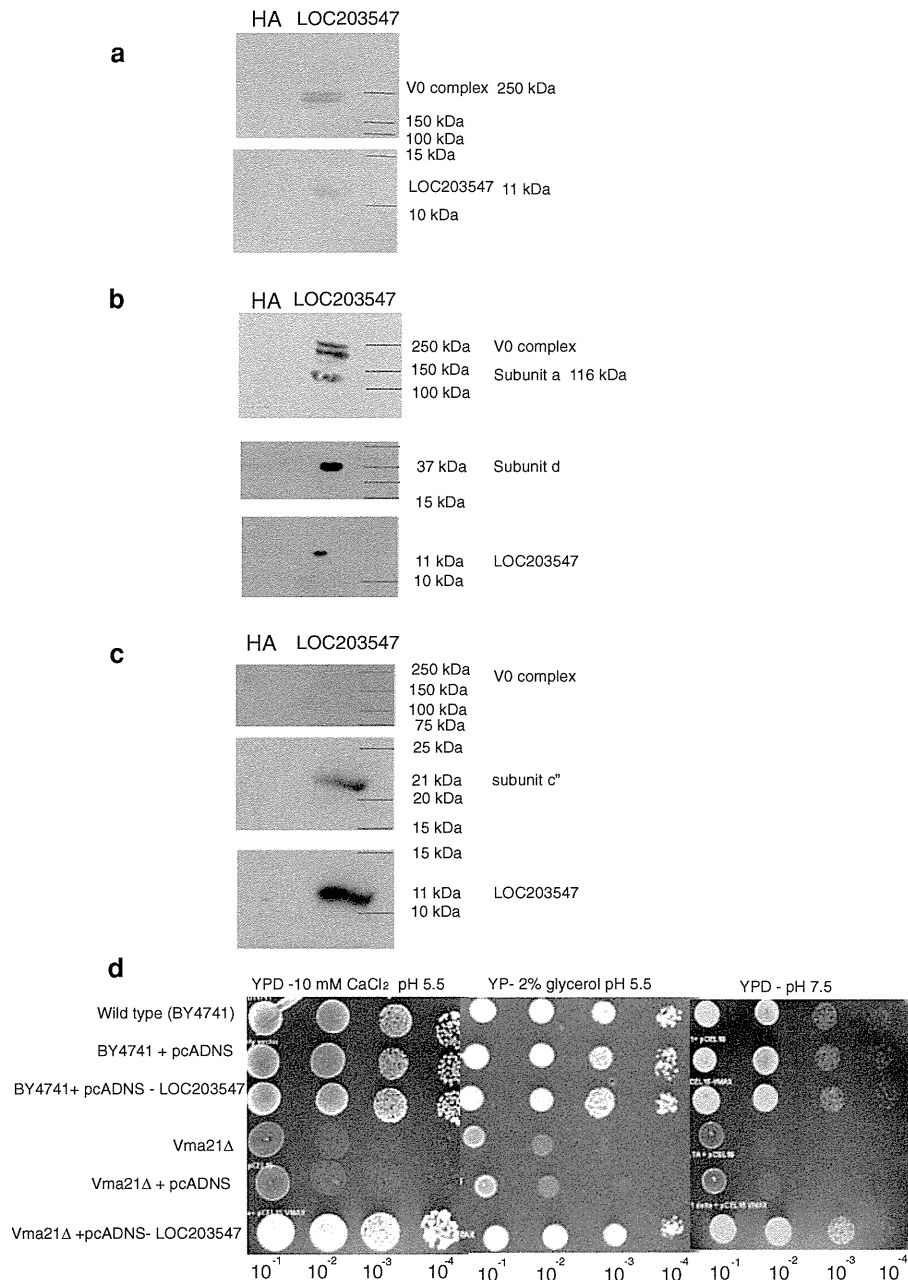
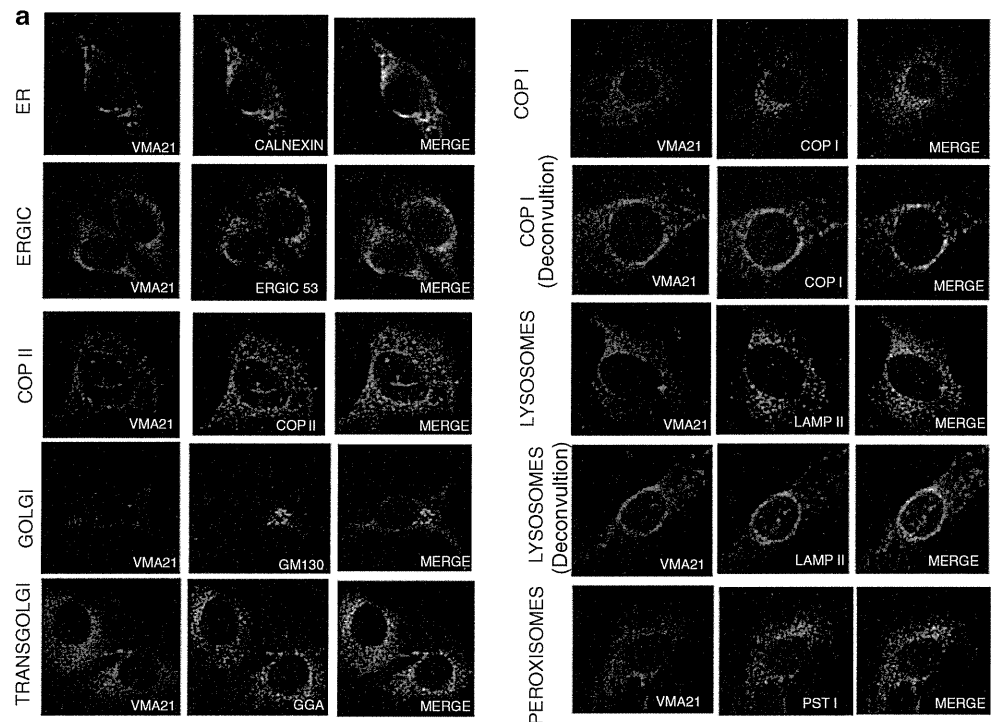


Fig. 4 LOC203547 interacts with V_0 via c'' , and LOC203547 rescues yeast *vma21Δ*. **a** LOC203547 antibody co-precipitates V_0 under non-denaturing conditions. Proteins from HEK293 cells solubilized in the presence of detergent C12E9 and DTSSP crosslinking were immunoprecipitated using an anti-LOC203547 antibody. The Western blot probed with anti-a antibody reveals the 250 kDa complete V_0 , indicating that LOC203547 interacts with V_0 . Subunit a is the dominant V_0 subunit (Supplemental Fig. 1). In yeast, V_0 assembly does not involve an initial interaction of Vma21p with subunit a, and Vma21p antibodies do not co-precipitate a except as part of intact V_0 (2). Absence of a 116 kDa band (subunit a) indicates that LOC203547 likewise does not separately interact with a. **b** When immunoprecipitation with the LOC203547 antibody was repeated in the presence of

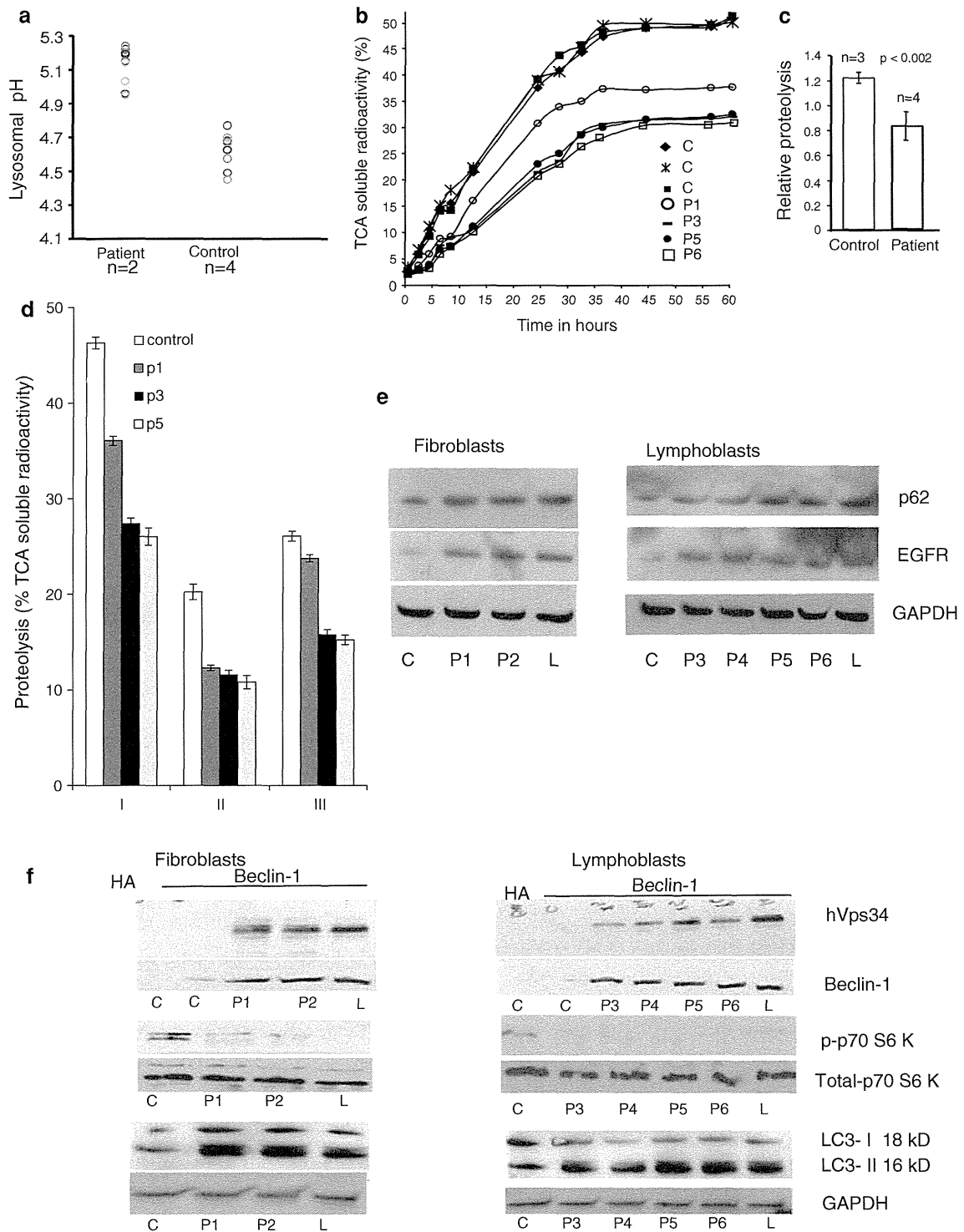
C12E9 but no crosslinking, the 250 kDa V_0 complex and subunits a (116 kDa) and d (37 kDa) were detected. Under these conditions, some amounts of at least these two subunits separates from the complex during SDS-PAGE, enabling their detection. **c** Under full denaturing conditions (no C12E9 and DTSSP crosslinking), immunoprecipitation using LOC203547 antibody and western blot using an antibody that recognizes both subunits c and c'' detects only the 21 kDa c'' subunit, no 250 kDa V_0 band, and no 16 kDa band corresponding to subunit c. **d** Comparison of growth patterns of yeast strains BY4741 (wild-type), *vma21Δ*, LOC203547-transformed *vma21Δ*, and controls. Successive dilutions (10^{-1} - 10^{-4}) of synchronously grown cultures of each strain plated in three different growth media. LOC203547 rescues the *vma21Δ* growth defect

Fig. 5 Intracellular localization of VMA21. **a** Human fibroblasts were treated with VMA21 antibody and co-stained with antibodies against compartment-specific markers. *Yellow fluorescence* indicates co-localization. Standard confocal and deconvolution microscopy were performed. The former is shown for all structures. Deconvolution microscopy, which reduces false co-localization in situations of highly abundant signal, as was the case for lysosomes (LAMP2) and COPI vesicles, is also shown for the latter two compartments. VMA21 localizes at the ER, the ERGIC, and on COPII vesicles. **b** Electron micrograph of VMA21 immunogold labeled ultrathin cryosection of a C2C12 cell. Note the *black dots (gold particles)* at the ER (*upper arrow*) and ER terminal cisternae (*lower arrow*) but not on mitochondrion (*arrowhead*); *Bar 0.25 μ m*



adenine, a specific macroautophagy inhibitor. We found that in controls and patients approximately half of long-lived protein degradation was macroautophagic and half through non-macro autophagy, that total long-lived protein degradation in patients was reduced by 25–50 % compared to controls, and that this reduction in autophagic flux was due approximately equally to reductions in macro and non-macro autophagies (Fig. 6b–d). Consistent with impaired macroautophagy, EGFR and p62, specific macroautophagy substrate proteins, accumulated in patient cells (Fig. 6e). In

separate experiments, proteolysis of short-lived proteins, which is largely non-lysosomal, was unaffected (not shown). We reasoned that a block in the final degradative stage of autophagy might induce a feedback upregulation of macroautophagy, i.e., increased autophagic signaling and increased autophagosome formation to overcome the end degradative block. Beclin-1 is a pivotal early component of autophagic signaling; its increase and increased interaction with the class III PI3 kinase hVps34 leads to activation and upregulation of the macroautophagy



pathway [4]. LC3 is a cytosolic protein which upon activation of macroautophagy converts from its LC3-I (18 kDa) to its LC3-II (16 kDa) form to function in the isolation membrane that forms the autophagosome [21]. Western blot and immunoprecipitation studies in fibroblasts and lymphoblasts showed major increases in beclin-1, beclin-1-hVps34 interaction, and LC3-II in XMEA

patients (Fig. 6f). LC3 was also increased at the transcriptional level, two-fold. The mRNA of a second early macroautophagy gene tested, *ATG12*, was increased ten-fold (Supplemental Fig. 9a). These results confirm that macroautophagy is upregulated in XMEA. We then tested the phosphorylation state of the p70S6 kinase and found it to be dephosphorylated (Fig. 6f) indicating that the

Fig. 6 Increased lysosomal pH, decreased protein degradation, and increased macroautophagy. **a** Spread of lysosomal pH values in patient and control fibroblasts; each small circle is the mean pH measurement of 10 lysosomes per cell. **b** Chase of lysosome-dependent long-lived protein degradation in lymphoblasts. **c** Average rates of proteolysis in patients determined by calculation of slopes of the linear phases in **(b)** and expressed relative to control samples. *Error bars* show standard deviation, and *p* values were calculated using *t* Test. **d I**, 36-hour time points from panel **b**. **II**, Cells cultured with macroautophagy inhibitor 3-MA, measures non-macroautophagic portion of lysosome-dependent proteolysis. **III**, Difference between **I** and **II**, i.e., between total lysosome-dependent proteolysis and its non-macro autophagic portion; measures the macroautophagic portion. *Error bars* mean \pm standard deviation of three independent repeats except for P5 bars **II** and **III** which are from two independent repeats. **e** Blocked degradative phase of macroautophagy in XMEA cells as evidenced by accumulation of the macroautophagy substrates EGFR and p62. Band intensities calculated using Image J: p62 in patient fibroblasts 0.48 ± 0.03 and 0.25 ± 0.008 in controls; EGFR in patient fibroblasts 0.277 ± 0.02 and 0.135 ± 0.009 in controls; p62 in patient lymphoblasts 0.45 ± 0.05 and 0.22 ± 0.07 in controls; EGFR in patient lymphoblasts 0.42 ± 0.02 and 0.14 ± 0.03 in controls. **f** Macroautophagic upregulation in XMEA cells (P1-P6) and low-dose leupeptin-treated non-XMEA cells (L); hVps34-beclin-1 interaction complexes were precipitated using a beclin-1 antibody followed by Western blotting for hVps34 and beclin-1: *Two upper panels*: both hVps34-beclin-1 are increased in patients and leupeptin-treated fibroblasts and lymphoblasts. Phosphorylation state of the p70S6 kinase determined by using phospho-specific (p-p70S6 K) and total p70S6 kinase antibodies: *Two middle panels*: p70S6 kinase is hypophosphorylated in patients and leupeptin-treated cells while the total p70S6 kinase levels remain similar. The mean intensities of p-p70 S6 K bands in fibroblasts: patients 0.060 ± 0.005 and controls 0.433 ± 0.010 ; in lymphoblasts: patients 0.149 ± 0.07 and controls: 1.04 ± 0.07 ; *Two lower panels*: Immunoblot of LC3: LC3-II concentrations are increased in patients and leupeptin-treated cells. Mean LC3-II: GAPDH band intensity ratios measured using Image J: 1.42 in patient vs. 0.17 in control fibroblasts. 0.707 in patient versus 0.079 in control lymphoblasts. LC3 mRNA quantifications are shown in Supplemental Fig. 9a, and LC3 immunocytochemistry in Supplemental Fig. 9b

mTORC1 pathway is inhibited, and that the XMEA autophagic upregulation is at least in part through mTORC1 inhibition.

The mTORC1 pathway is chiefly inhibited (i.e., autophagy is activated) by reduced levels of cellular amino acids [1], which we measured and found to be $\sim 50\%$ lower in XMEA than in control fibroblasts (Fig. 7a). Leucine is the principal amino acid involved in mTORC1 regulation [1, 2]. We measured its level specifically and found it reduced by over 50% (Fig. 7b). Finally, supplementing the media with 10X leucine methyl ester (final concentration of 0.05 mM), a form of leucine that diffuses freely into cells [38], corrected the p70S6 kinase phosphorylation (Fig. 7c). Together, these results indicate that reduced cellular amino acids are at least in part the cause of autophagic activation in XMEA. Interestingly, while supplementing the media with normal leucine also corrected the phosphorylation status of the p70S6 kinase (Fig. 7d), it did not do so to the level of normal cells suggesting that

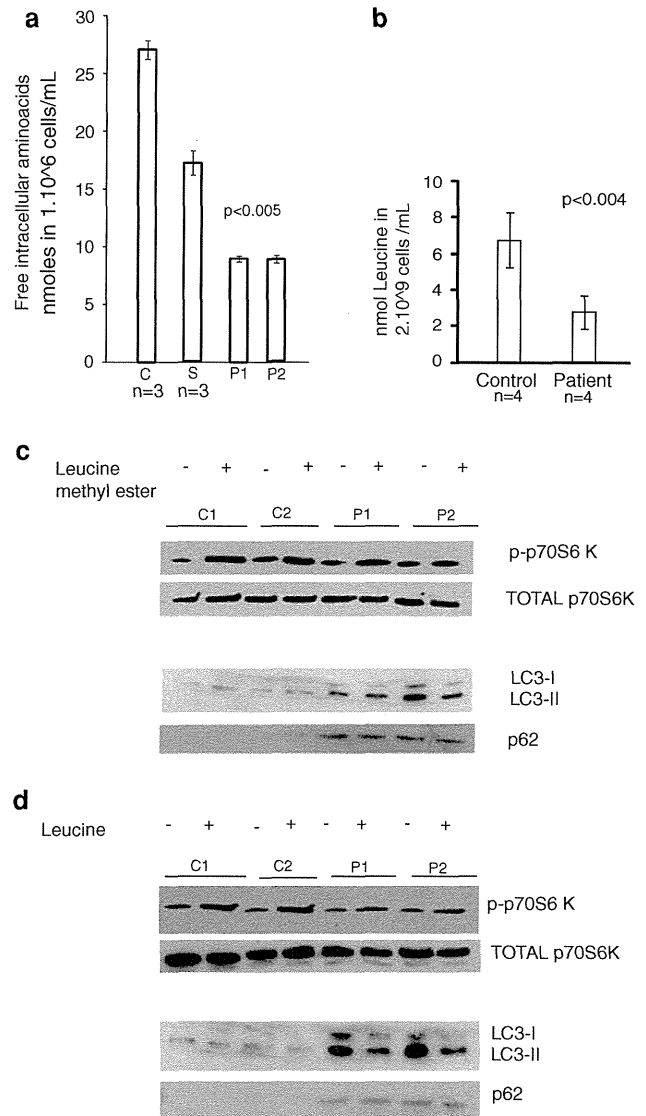


Fig. 7 Decreased intracellular amino acids and correction of autophagic upregulation by leucine esters. **a** Quantitation of intracellular free amino acids; C control fibroblasts; S control fibroblasts in starvation condition (Hanks balanced salt solution for 4 h); C and S are pooled results from three separate fibroblast lines each measured three times. Note, XMEA cells maintain themselves at even lower free amino acid concentration than the starved control cells. *Error bars* mean \pm standard error on triplicate readings. **b** Quantitation of intracellular leucine in control ($n = 4$) and patient ($n = 4$) fibroblasts using LC-MS. *Error bars* show standard deviation from three independent repeats. **c** Phosphorylation status of p70S6 kinase is restored in patients treated with leucine methyl ester. **d** Phosphorylation status of p70S6 kinase is partially restored in patient cells treated with leucine

leucine transport is decreased in XMEA, which, we hypothesize, is likely physiologic (see “Discussion”).

Autolysosomes are evanescent structures that rapidly degrade their contents, and few are observed in normal cells at any one time. We asked whether in XMEA the upregulation of macroautophagy, coupled with delayed

Fig. 8 Morphological Features of XMEA Fibroblasts (see also Supplemental Fig. 8).

a Fibroblast from an unaffected individual; *bar* 2 μm .

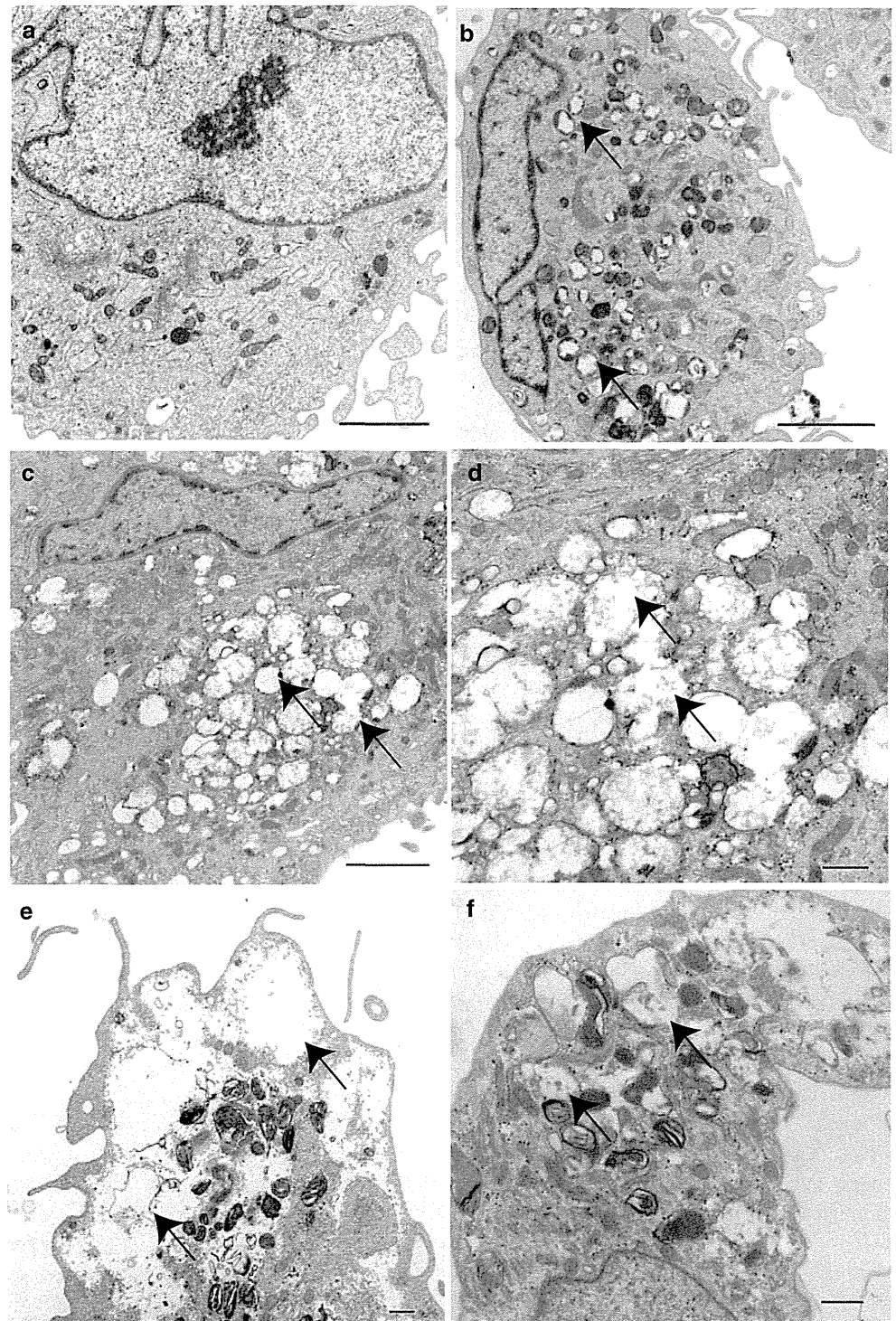
b Representative example of the most common appearance in patient fibroblasts; extensive number of autolysosomes distributed throughout the cell; *bar* 2 μm .

c Autolysosomes in a fibroblast from an affected individual merging to form autophagic vacuoles. This was noted in 11 of 100 consecutive fibroblasts examined from two patients; *bar*, 2 μm .

d Higher power of (C); *bar* 0.5 μm .

e Extreme example of giant autophagic vacuolation in a fibroblast from an affected patient; *bar* 0.5 μm .

f Representative non-XMEA normal fibroblast treated with leupeptin exhibits the morphological characteristics of XMEA; *bar* 0.5 μm



degradation of autolysosomal contents, results in increased autolysosomes. Electron and immunofluorescence microscopy showed a proliferation of autolysosomes in XMEA lymphoblasts, fibroblasts, leukocytes, and platelets (examples from fibroblasts shown in Fig. 8 and Supplemental Figs. 2g, 10). Cells were otherwise morphologically normal, except in a minority, counted at

~10 % in fibroblasts, where the numerous autolysosomes were observed merging one with the other forming large vacuoles comparable to the disease-defining autophagic vacuolation of XMEA skeletal muscle (Fig. 8c–e). These observations show that cells other than muscle also exhibit autophagic vacuolation in XMEA, although seemingly in lesser proportions (10 % in fibroblasts, present study, vs.

40–80 % in skeletal muscle [12, 36]). Further, the electron micrograph data is consistent with a progression from upregulated autophagy to proliferation of autolysosomes and finally to autophagic vacuolation.

We aimed to determine whether VMA21 mutations cause the above succession of events through the block in the final degradative stage of autophagy, and not through a separate mechanism, i.e., we asked whether blocking the degradative stage by 25–50 %, alone, elicits macroautophagy, and autophagic vacuolation. Leupeptin is a pH-independent inhibitor of lysosomal hydrolases and, therefore, of the degradative stage of autophagy. First, we determined 30 μ M as the leupeptin concentration needed to decrease long-lived protein degradation by 37 % (Supplemental Fig. 11). Lymphoblasts and fibroblasts from normal subjects incubated with this concentration of leupeptin exhibited decreased mTORC1 dependent upregulation of autophagic signaling (Fig. 6f), and autolysosome proliferation, autolysosome mergers, and autophagic vacuolation (Fig. 8f), similar to XMEA.

Restoring VMA21 mRNA levels corrects the XMEA autophagic disturbance

As final proofs that decreased VMA21 is the cause of the autophagic disturbance in XMEA, we performed the following experiments. We reduced *Vma21* mRNA in NIH 3T3 cells by silencing with *Vma21* RNAi and observed appearance of the typical XMEA vacuolation (Fig. 9a, b). Next, we raised the levels of *Vma21* mRNA in XMEA fibroblasts by retroviral infection and stable expression of *Vma21*. This led to near-normalization of V-ATPase at protein level (Fig. 9c), its assembly (as shown by near-normalization of free cytosolic subunit E (Fig. 9d), V-ATPase activity (Fig. 9e), and lysosomal pH (not shown). As a consequence, there were improvements in long-lived protein degradation, LC3 isoform levels, beclin-1 levels, beclin-1-hVps34 interaction, and intracellular amino acid levels (Fig. 9f–i). Autolysosomes and autophagic vacuoles were no longer present and cells returned to normal morphology (Fig. 9j).

Not all V-ATPase dependent functions are affected in XMEA

Multiple cell functions other than autophagy require the V-ATPase, none of which appear to be affected to a clinical extent in our patients. We studied one of these systems, maturation of lysosomal enzymes which consists of stepwise proteolytic processing in compartments with decreasing pH set by increasing V-ATPase activity [32]. We examined hexosaminidases A and B and cathepsin D in XMEA fibroblasts, and found that maturation of all three, as

determined by polypeptide processing and in vitro activities, were identical to controls (Supplemental Fig. 12).

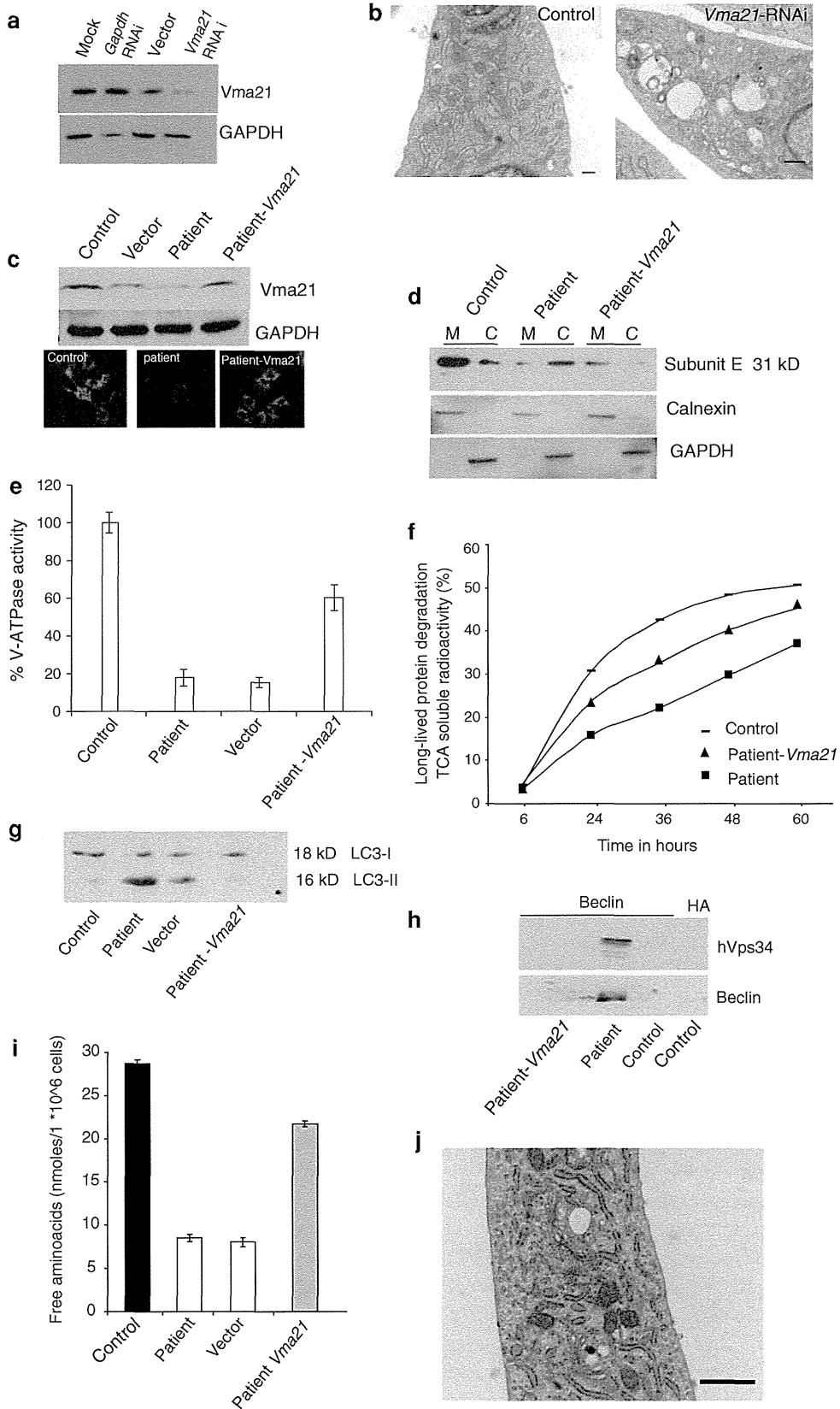
Discussion

XMEA mutations are hypomorphic alleles that reduce the amount of VMA21, in most cases by decreasing mRNA splicing efficiency. Only skeletal muscle is clinically affected and only in males. Female carriers are unaffected likely because muscle is a syncytium and half the nuclei will produce normal VMA21 mRNA amounts. We show that VMA21 is the human ortholog of the yeast V-ATPase chaperone Vma21p, and that reduced VMA21 results in reduced V-ATPase activity to 10–30 % of normal. The human proteome lacks the c' V-ATPase subunit with which the yeast Vma21p interacts. We find that human VMA21 interfaces with the V-ATPase through the c'' subunit, although it may well have additional contacts. VMA21 may also have functions other than assembling the V-ATPase, mediated through other interacting partners.

Several other genetic diseases affecting V-ATPases have been described. In these diseases, mutations affect particular V-ATPase subunits that confer subcellular location or tissue specificity and result in corresponding symptoms such as developmental delay with wrinkled skin syndrome (subunit a2) [14], osteopetrosis (subunit a3) [9], and renal tubular acidosis with deafness (subunit a4) [13]. XMEA is the first disease in which all V-ATPases are affected. On the other hand, XMEA mutations do not completely eliminate V-ATPase activity. XMEA patients do not exhibit neurodevelopmental delay or clinically manifest skin and bone abnormalities, acidosis, or hearing loss, indicating that for the specialized a2, a3, and a4-containing V-ATPases, the reduced V-ATPase assembly in XMEA does not reach clinical threshold.

The reduced V-ATPase activity in XMEA results in a rise in lysosomal pH from 4.7 to 5.2. Maturation and activities of three lysosomal enzymes tested are not affected in vitro. However, in vivo, these enzymes are expected to have lowered activity in patient lysosomes due to the raised pH. Hexosaminidase, e.g., is known to be 50 % less active at pH 5.2 than at 4.7 [32]. Not surprisingly, this degree of hexosaminidase downregulation is tolerated by XMEA patients because they, like Tay-Sachs disease carriers who also have 50 % reduced hexosaminidase, do not have Tay-Sachs symptoms. Other individual lysosomal enzymes are likely similarly subclinically affected.

The final stage of autophagy, i.e., the collective activity of lysosomal enzymes involved in the degradation of long-lived proteins, is also reduced. The extent of this reduction in patient cell lines is certainly greater than the 50 % we recorded, because, as we showed, it is coupled with a



◀**Fig. 9** Downregulating *Vma21* generates XMEA-like vacuolation in normal cells, and restoring *Vma21* mRNA levels in patient cells corrects the XMEA autophagic disturbance phenotypes. **a** Western blot with antibody against *Vma21* showing reduced *Vma21* in NIH 3T3 cells treated with *VMA21* RNAi; *mock lane* cells treated with transfection reagents with no vectors; *vector lane* same as mock but includes empty vector. **b** Electron micrograph of *Vma21* RNAi-treated NIH 3T3 cells shows typical vacuolation as in XMEA; *left panel* representative cell from empty vector transfection; *right panel* representative cell from *Vma21* siRNA transfection; *bar* 0.5 μ m. **c** HIV-mediated expression of *Vma21* followed by Western blotting (*top panel*) and immunofluorescence microscopy (*bottom panel*) using the *Vma21* antibody; *Control* cell line from unaffected individual with no treatment; *Vector XMEA* cell line treated with empty viral vector; *Patient XMEA* cell line untreated; *Patient-Vma21 XMEA* cell line treated with *Vma21* viral vector; retroviral expression method described in Supplement. **d** Improved V-ATPase assembly as verified by normalization of cytosolic Subunit E levels (Western blot with anti-E antibody); *M* membrane fraction and *C* cytosolic fraction. **e** Improved V-ATPase activity. **f** Improved long-lived protein degradation. **g** Correction of LC3. **h** Normalization of beclin and hVps34-beclin-1 interaction; anti-HA antibody immunoprecipitation control. **i** Correction of intracellular free amino acid level. **j** Normalization of cellular morphology and disappearance of autophagic vacuolation; representative patient cell following *Vma21* viral transfection; *bar* 0.5 μ m

compensatory upregulation of macroautophagy with which cells achieve the 50 % level. The block in the final stage of autophagy is likely at least in part the driver of the pre-degradative stages of autophagy that defines this disease. As we here, and others [15, 37], have shown direct inhibition of lysosomal hydrolases with leupeptin leads to mTORC1 inactivation-dependent upregulation of autophagy. Expected outcomes of blocked autophagy are reduced recycling of defective and unneeded proteins, and reduced generation of amino acids through this recycling. Reduced amino acids, specifically leucine, are the most potent inducer of macroautophagy, through inhibition of the mTORC1 pathway. Total cellular amino acids, including leucine, are reduced in XMEA cells by ~50 % and, therefore, the autophagic upregulation in this disease is at least in part due to amino acid insufficiency. This is confirmed by the correction of mTORC1 signaling with replenishment of leucine in the form of leucine esters. A second explanation for the autophagic activation in XMEA comes to light with recent elegant work showing that the V-ATPase, in the lysosomal membrane, plays a central role in the sensing of amino acid levels, and through direct interactions with Rag GTPases regulating the mTORC1 pathway [38]. Reduced V-ATPases would reduce mTORC1 activation, which in turn activates autophagy. This direct function of the V-ATPase in regulating autophagy, like other V-ATPase functions, appears to be only partially eliminated in our patients, as evidenced by the correctability of the autophagic upregulation when an excess of leucine esters is added to the cell media.

Why do amino acids, including leucine, remain low in XMEA cells, despite their abundance in culture media (or through nutrition in the patients), i.e., why do XMEA cells not replenish their amino acids from the media? We speculate that this is a physiological response. If the cells were to fully replace their amino acid shortfalls resulting from the autophagic defect with extrinsic amino acids they would continually acquire net surpluses of proteins which would increasingly tax already strained autophagy. The cells may have adapted to a new homeostasis that allows survival in a starvation-equivalent mode rather than demise through total autophagic failure. Consistent with a reduction in amino acid uptake is our observation that leucine proper which requires active transport, only partially rescues the mTORC1 pathway inactivation in these cells, compared to leucine ester, which does not require active transport. It is, of course, also possible that the putative amino acid transport defect is pathologic, a component of the disease that requires future elucidation.

Increased macroautophagy means increased formation of autolysosomes, but in XMEA each new autolysosome formed faces a degradative block and is slow to progress and disappear. We theorize that increased formation coupled with delayed progression results in vast numbers of autolysosomes, which fusing together form the giant autophagic vacuoles that characterize the disease.

We posited that the autophagic block is a consequence of decreased V-ATPase activity. The possibility exists that it is instead caused by some other effect of the *VMA21* mutations unrelated to their effect on the V-ATPase. This is ruled out by the following. Bafilomycin is a specific inhibitor of the V-ATPase. At concentrations above 10 nM, it completely inhibits V-ATPase activity. Between 0.3 and 10 nM it reduces V-ATPase activity to 10–40 % of normal [7], similar to the V-ATPase activity in XMEA. There are several reports in the literature in which, as controls for other experiments, cells of various types were treated with these low concentrations of bafilomycin. This resulted in decreased autophagy, mTORC1 inactivation-dependent activation of macroautophagy, and autolysosome proliferation and autophagic vacuolation [25, 31], which upon review are identical to what we observe in XMEA. V-ATPase blockage, therefore, has the same outcome as *VMA21* mutations, confirming that the mutations cause the autophagic defect via their effect on the V-ATPase. The literature also substantiates that decreased V-ATPase causes the autophagic block through raising lysosomal pH. Chloroquine and siramesine are agents that accumulate in lysosomes, raise lysosomal pH, block autophagy, and lead to mTORC1 inactivation-dependent macroautophagy and autophagic vacuolation [25, 31, 33]. Chloroquine is in clinical use as an antimalarial and antirheumatic agent.

Prolonged exposure to chloroquine causes an iatrogenic disease clinically affecting only skeletal muscle, and retina despite the fact that lysosomes of all tissues are affected. This disease is an autophagic vacuolar myopathy that is so similar to XMEA that it is its main pathological differential diagnosis [12, 33]. Finally, that autophagic block is at least in part the cause of the macroautophagic upregulation and autophagic vacuolation, is demonstrated in this study.

Apart from chloroquine myopathy, the differential diagnosis of XMEA includes Danon disease, which results from LAMP2 deficiency [24]. LAMP2 is a lysosomal membrane protein that participates in chaperone-mediated autophagy, lysosome biogenesis, lysosome-autophagosome fusion, and lysosome locomotion along microtubules toward phagosomes [17]. Defects in any or all of these processes could reduce degradative autophagy and underlie the vacuolation in Danon disease. In fact, in the mouse model of this disease, organs with impaired long-lived protein degradation are the ones that exhibit autophagic vacuolation [34]. As such, the pathogenesis of both major forms of vacuolar myopathy, Danon disease, and XMEA would include a block in the degradative phase of autophagy, in Danon disease due to the loss of the above lysosomal functions, in XMEA due to lost V-ATPase activity. We did verify that Danon disease is not associated with V-ATPase deficiency (Supplemental Fig. 13).

Presence of autophagic vacuolation in all XMEA cell types studied to date indicates that the disease is likely subclinically widespread. Why only skeletal muscle is affected clinically is unknown. This does not appear to be due to a greater reduction in V-ATPase activity in muscle compared to other tissues (Fig. 3a, b). The greater autophagic vacuolation in skeletal muscle where 40–80 % of cells are affected [12, 36] compared to the 10 % affected cells in other tissues studied in this work, suggests that skeletal muscle might be reacting more vigorously to the blocked autophagy than other tissues. In fact, macroautophagy in skeletal muscle is characterized by the particularity of a vastly greater macroautophagic response to decreased amino acids compared to other tissues, the purpose of which is to break itself down to supply amino acids to other organs [22, 29]. This enhanced response is mediated through mTORC1 inactivation, as in other tissues, but also through a second much more potent muscle-specific pathway, FoxO3 [19]. This drastic macroautophagic response is highest in type II fast-twitch fibers [16, 22], which are the fibers with the highest degree of autophagic vacuolation and atrophy in XMEA [12, 36].

This work describes the clinical outcome at the cusp of tolerable reduction in V-ATPase. Beyond XMEA, it has implications for other, much more common, diseases. In malaria, the parasite inserts a V-ATPase into the erythrocyte membrane conferring itself optimal pH, and increased

V-ATPase activity is an important component of HIV infection, osteoporosis, and cancer metastasis [8]. Our XMEA patients show that the safety margin of reducing V-ATPase activity in humans is wide, increasing the potential to utilize bafilomycin-related compounds, or RNAi against VMA21, as possible therapies against a host of diseases processes that rely on the V-ATPase.

Acknowledgments We wish to thank all the XMEA families. We are grateful to Drs. G. Israelian, V.C. Juel, M. Villanova, the late G. Karpati, S. Carpenter, and D. Figarella-Branger for the clinicopathologic diagnosis of some of the patients included in this study, previously published in clinical journals. We thank Drs. S. Grinstein for helpful discussions and Drs. J Rommens and S Meyn for their review of our manuscript, T. Sarkisyan, J. Kere, E. Heon, F. Zara and H. Lohi for ethnic control DNA samples, A. Leung for assistance with experiments in Supplemental Fig. 12, N. Ochtony for Supplemental Fig. 1A, P. Bradshaw for assistance in deconvolution microscopy. Principal funding was from the Canadian Institutes of Health Research. The Association Française contre les Myopathies provided support to N. Levy, EVO Funds of Helsinki and Turku University Hospitals (Finland) and sports research grant from Ministry of Education of Finland to H. Kalimo, and the Natural Sciences and Engineering Research Council (Canada) to I. Munteanu.

Conflict of interest The authors declare that they have no conflicts of interests.

Ethical standard This study was approved by the Research Ethics Board of the Hospital for Sick Children Toronto and informed consent was obtained from all subjects.

References

1. Beugnet A, Tee AR, Taylor PM, Proud CG (2003) Regulation of targets of mTOR (mammalian target of rapamycin) signalling by intracellular amino acid availability. *Biochem J* 372:555–566
2. Blommaert EF, Luiken JJ, Blommaert PJ, van Woerkom GM, Meijer AJ (1995) Phosphorylation of ribosomal protein S6 is inhibitory for autophagy in isolated rat hepatocytes. *J Biol Chem* 270:2320–2326
3. Brummelkamp TR, Bernards R, Agami R (2002) A system for stable expression of short interfering RNAs in mammalian cells. *Science* 296:550–553
4. Cao Y, Klionsky DJ (2007) Physiological functions of Atg6/Beclin 1: a unique autophagy-related protein. *Cell Res* 17:839–849
5. Cuervo AM, Stefanis L, Fredenburg R, Lansbury PT, Sulzer D (2004) Impaired degradation of mutant alpha-synuclein by chaperone-mediated autophagy. *Science* 305:1292–1295
6. Demarex N, Furuya W, D'Souza S, Bonifacino JS, Grinstein S (1998) Mechanism of acidification of the trans-Golgi network (TGN). In situ measurements of pH using retrieval of TGN38 and furin from the cell surface. *J Biol Chem* 273:2044–2051
7. Droese S, Altendorf K (1997) Bafilomycins and concanamycins as inhibitors of V-ATPases and P-ATPases. *J Exp Biol* 200:1–8
8. Forgacs M (2007) Vacuolar ATPases: rotary proton pumps in physiology and pathophysiology. *Nat Rev Mol Cell Biol* 8: 917–929
9. Frattini A, Orchard PJ, Sobacchi C et al (2000) Defects in TCIRG1 subunit of the vacuolar proton pump are responsible for

- a subset of human autosomal recessive osteopetrosis. *Nat Genet* 25:343–346
10. Fukuda K, Hirai Y, Yoshida H, Nakajima T, Usui T (1982) Free amino acid content of lymphocytes and granulocytes compared. *Clin Chem* 28:1758–1761
 11. Huss M, Sasse F, Kunze B (2005) Archazolid and apicularen: novel specific V-ATPase inhibitors. *BMC Biochem* 6:13
 12. Kalimo H, Savontaus ML, Lang H et al (1988) X-linked myopathy with excessive autophagy: a new hereditary muscle disease. *Ann Neurol* 23:258–265
 13. Karet FE, Finberg KE, Nelson RD et al (1999) Mutations in the gene encoding B1 subunit of H⁺-ATPase cause renal tubular acidosis with sensorineural deafness. *Nat Genet* 21:84–90
 14. Kornak U, Reynders E, Dimopoulou A et al (2008) Impaired glycosylation and cutis laxa caused by mutations in the vesicular H⁺-ATPase subunit ATP6V0A2. *Nat Genet* 40:32–34
 15. Kovacs AL, Reith A, Seglen PO (1982) Accumulation of autophagosomes after inhibition of hepatocytic protein degradation by vinblastine, leupeptin or a lysosomotropic amine. *Exp Cell Res* 137:191–201
 16. Li JB, Goldberg AL (1976) Effects of food deprivation on protein synthesis and degradation in rat skeletal muscles. *Am J Physiol* 231:441–448
 17. Malicdan MC, Noguchi S, Nonaka I, Saftig P, Nishino I (2008) Lysosomal myopathies: an excessive build-up in autophagosomes is too much to handle. *Neuromuscul Disord* 18:521–529
 18. Malkus P, Graham LA, Stevens TH, Schekman R (2004) Role of Vma21p in assembly and transport of the yeast vacuolar ATPase. *Mol Biol Cell* 15:5075–5091
 19. Mammucari C, Schiaffino S, Sandri M (2008) Downstream of Akt: foxO3 and mTOR in the regulation of autophagy in skeletal muscle. *Autophagy* 4:524–526
 20. Massey AC, Kaushik S, Sovak G, Kiffin R, Cuervo AM (2006) Consequences of the selective blockage of chaperone-mediated autophagy. *Proc Natl Acad Sci USA* 103:5805–5810
 21. Mizushima N (2007) Autophagy: process and function. *Genes Dev* 21:2861–2873
 22. Mizushima N, Yamamoto A, Matsui M, Yoshimori T, Ohsumi Y (2004) In vivo analysis of autophagy in response to nutrient starvation using transgenic mice expressing a fluorescent autophagosome marker. *Mol Biol Cell* 15:1101–1111
 23. Munteanu I, Ramachandran N, Mnatzakanian GN et al (2008) Fine-mapping the gene for X-linked myopathy with excessive autophagy. *Neurology* 71:951–953
 24. Nishino I, Fu J, Tanji K et al (2000) Primary LAMP-2 deficiency causes X-linked vacuolar cardiomyopathy and myopathy (Danon disease). *Nature* 406:906–910
 25. Ostefeld MS, Hoyer-Hansen M, Bastholm L et al (2008) Anti-cancer agent siramesine is a lysosomotropic detergent that induces cytoprotective autophagosome accumulation. *Autophagy* 4:487–499
 26. Paroutis P, Touret N, Grinstein S (2004) The pH of the secretory pathway: measurement, determinants, and regulation. *Physiology (Bethesda)* 19:207–215
 27. Salvador N, Aguado C, Horst M, Knecht E (2000) Import of a cytosolic protein into lysosomes by chaperone-mediated autophagy depends on its folding state. *J Biol Chem* 275:27447–27456
 28. Sandri M (2010) Autophagy in skeletal muscle. *FEBS Lett* 584:1411–1416
 29. Scornik OA, Howell SK, Botbol V (1997) Protein depletion and replenishment in mice: different roles of muscle and liver. *Am J Physiol* 273:E1158–E1167
 30. Scott JA, North ML, Rafii M et al (2011) Asymmetric dimethylarginine is increased in asthma. *Am J Respir Crit Care Med* 184:779–785
 31. Shacka JJ, Klocke BJ, Shibata M et al (2006) Bafilomycin A1 inhibits chloroquine-induced death of cerebellar granule neurons. *Mol Pharmacol* 69:1125–1136
 32. Sharma R, Deng H, Leung A, Mahuran D (2001) Identification of the 6-sulfate binding site unique to alpha-subunit-containing isozymes of human beta-hexosaminidase. *Biochemistry* 40:5440–5446
 33. Stauber WT, Hedge AM, Trout JJ, Schottelius BA (1981) Inhibition of lysosomal function in red and white skeletal muscles by chloroquine. *Exp Neurol* 71:295–306
 34. Tanaka Y, Guhde G, Suter A et al (2000) Accumulation of autophagic vacuoles and cardiomyopathy in LAMP-2-deficient mice. *Nature* 406:902–906
 35. Taussky HH, Shorr E (1953) A microcolorimetric method for the determination of inorganic phosphorus. *J Biol Chem* 202:675–685
 36. Villanova M, Louboutin JP, Chateau D et al (1995) X-linked vacuolated myopathy: complement membrane attack complex on surface membrane of injured muscle fibers. *Ann Neurol* 37:637–645
 37. Webber JL, Tooze SA (2010) Coordinated regulation of autophagy by p38alpha MAPK through mAtg9 and p38IP. *EMBO J* 29:27–40
 38. Zoncu R, Bar-Peled L, Efeyan A, Wang S, Sancak Y, Sabatini DM (2011) mTORC1 senses lysosomal amino acids through an inside-out mechanism that requires the vacuolar H(+)-ATPase. *Science* 334:678–683

Lysosomal storage and advanced senescence in the brain of LAMP-2-deficient Danon disease

Akiko Furuta · Koichi Wakabayashi · Joji Haratake · Hisae Kikuchi · Tomohiro Kabuta · Fumiaki Mori · Fusao Tokonami · Yukinori Katsumi · Fumihiko Tanioka · Yasuo Uchiyama · Ichizo Nishino · Keiji Wada

Received: 21 September 2012/Revised: 13 December 2012/Accepted: 14 December 2012
© Springer-Verlag Berlin Heidelberg 2012

Danon et al. first described two 16-year-old boys with cardiomegaly, proximal myopathy and mental retardation as “lysosomal glycogen storage disease with normal acid maltase” in 1981 [2]. In 2000, Nishino et al. [6] identified that lysosome-associated membrane protein type 2 (LAMP-2) is the responsible gene for Danon disease. Despite the presence of mental retardation, the neuropathological findings have not yet been described. Moreover, one of the splice-variants, LAMP-2A, serves as a receptor for chaperone-mediated autophagy (CMA) which is implicated in neurodegenerative disorders [1]. Here we report an autopsy case of genetically confirmed Danon disease with an exon-6-skipping mutation (Nishino et al., patient 3) [6]. A genetic confirmation of LAMP-2 deficiency and clinical manifestations of this case were

described previously [4, 6]. Briefly, he was born at full-term without any abnormalities. In childhood, he was in low-performing schools. At age of 22, dilated cardiomyopathy was diagnosed and a pacemaker was implanted. At age of 26, the full-scale intelligence quotient was 60. He expired from cardiac failure at age of 31. His mother had been diagnosed with cardiomyopathy and liver disease, and had died of heart failure at age of 52.

The macroscopic appearance of the brain did not exhibit any abnormality. Microscopically, pale granular neurons were found particularly in the nucleus basalis of Meynert and cranial nerve nuclei such as oculomotor, dorsal vagal and hypoglossal nuclei (Fig. 1b–d, k; Suppl Table 1). Although neuronal loss was not noted, mild astrocytosis was seen in the basal ganglia, hippocampus and brainstem. In addition, neurons containing lipofuscin-like granules were remarkable (Suppl. Table 1). The distribution of these neurons was different from that of pale

Electronic supplementary material The online version of this article (doi:10.1007/s00401-012-1075-4) contains supplementary material, which is available to authorized users.

A. Furuta (✉) · Y. Uchiyama
Department of Cell Biology and Neuroscience,
Juntendo University Graduate School of Medicine,
Hongo 2-1-1, Bunkyo-ku, Tokyo 113-8421, Japan
e-mail: afuruta@juntendo.ac.jp

A. Furuta · H. Kikuchi · T. Kabuta · K. Wada
Department of Degenerative Neurological Diseases,
National Institute of Neuroscience, National Center of
Neurology and Psychiatry, Tokyo, Japan

K. Wakabayashi · F. Mori
Department of Neuropathology, Institute of Brain Science,
Hirosaki University Graduate School of Medicine,
Hirosaki, Japan

J. Haratake
Department of Laboratory Medicine, Saiseikai Yahata General
Hospital, Kitakyushu, Japan

F. Tokonami
Department of Neurology, Hamamatsu Rosai Hospital,
Hamamatsu, Japan

Y. Katsumi
Moriyama Sakura Medical Clinic, Moriyama, Japan

F. Tanioka
Division of Pathology and Laboratory Medicine, Iwata City
Hospital, Iwata, Japan

I. Nishino
Department of Neuromuscular Research, National Institute
of Neuroscience, National Center of Neurology and Psychiatry,
Tokyo, Japan

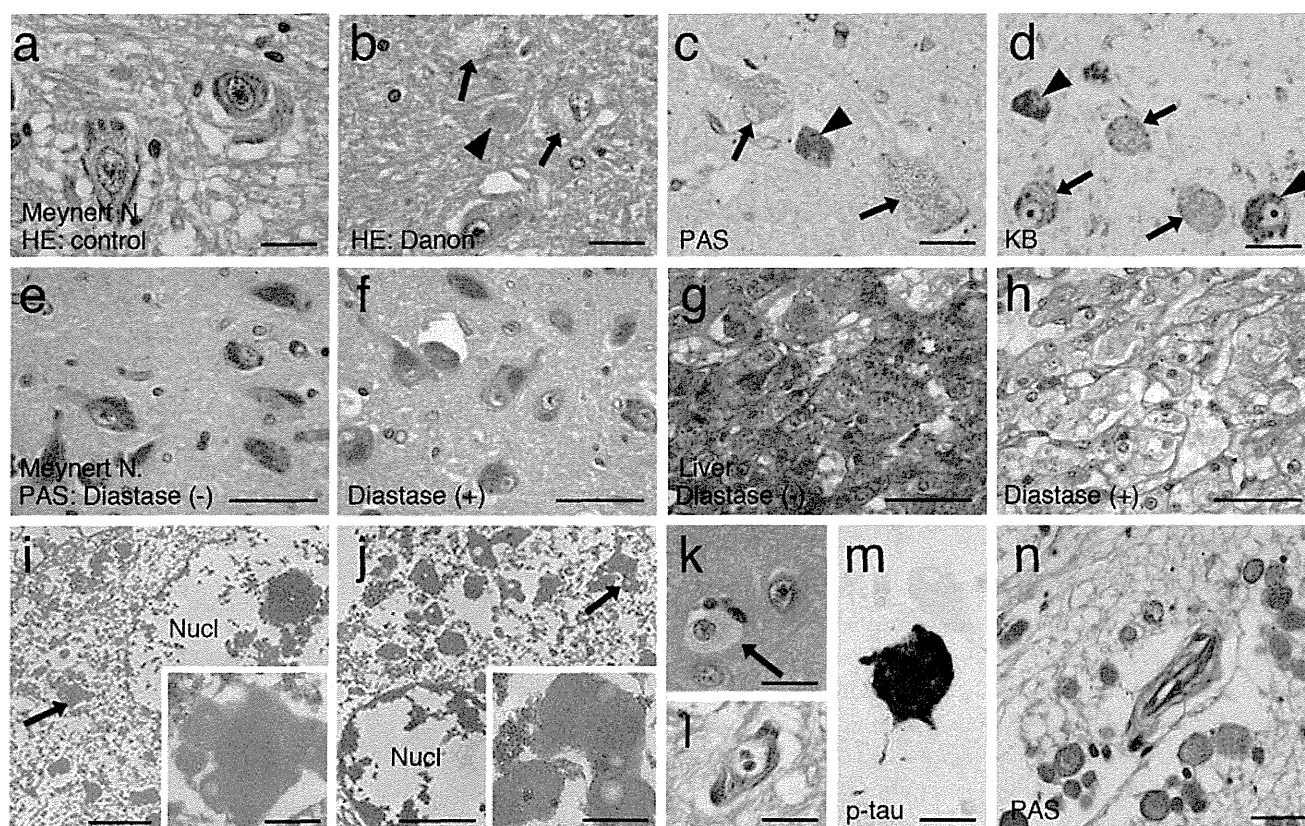


Fig. 1 Histopathological findings in Danon disease. The basal nucleus of Meynert from an age-matched control case (34-year-old male) (**a**) and Danon disease (**b–d**). Pale granular neurons (*arrows*) and lipofuscin-like granule-laden neurons (*arrowheads*). **a, b** HE, **c** PAS, **d** KB. The basal nucleus (**e, f**) and liver (**g, h**) stained with PAS in Danon disease. PAS-positive granules are preserved after diastase digestion in the brain (**f**), but not in the liver (**h**). **i, j** Electron-dense materials with small vacuoles in the neuronal cytoplasm in the

basal nucleus (*arrows*, Nucl, nucleus). **k** Rare occurrence of pale granular neurons in the frontal cortex. HE: **l** Marinesco body-containing pigmented neurons in the substantia nigra. HE: **m** Phosphorylated tau-immunoreactive neurons in the oculomotor nucleus. **n** A large number of corpora amylacea in the subpial and perivascular regions in the frontal base. PAS: Bars 25 μm (**a–d, k–m**), 50 μm (**e–h**), 3 μm (**i, j**) and 500 nm (*insets* of **i, j**)

granular neurons. The lipofuscin-like granules were positive for periodic acid-Schiff (PAS) and Luxol fast-blue in Klüver-Barrera (KB) staining (Fig. 1c, d). Diastase digestion tests revealed that PAS-positive granules in neurons were not digestible, whereas those in hepatocytes were digestible indicating accumulation of glycogen in the liver (Fig. 1e–h). Electron microscopy showed accumulations of electron-dense materials in the neuronal cell bodies (Fig. 1i, j). Marinesco body-containing pigmented neurons were frequently seen in the substantia nigra (Fig. 1l). A few neurofibrillary tangles were seen in the oculomotor nucleus and locus ceruleus (Fig. 1m); however, no amyloid plaques or α -synucleinopathy lesions were found in the brain. The number of corpora amylacea was apparently increased compared with age-matched controls ($n = 5$) ranging in age from 27 to 38 years (Fig. 1n). Several axonal spheroids were observed in the gracile nuclei. Pale granular neurons in the basal nucleus of Meynert were not immunoreactive for macroautophagy

marker, LC-3 and faintly immunoreactive for ubiquitin, whereas immunoreactivity for both LC-3 and ubiquitin was enriched in the vacuolated cardiomyocytes (Suppl. Fig. 1). Major pathological findings of the visceral organs were extensive cardiomyopathy and liver cirrhosis (Suppl. Fig. 2, 3).

Since glycogen accumulation or autophagic vacuoles were not observed, the neuropathological findings in our case are different from those in the brain of acid maltase deficiency (Pompe disease) as well as in the heart and skeletal muscles of Danon disease. These cell-type specific alterations in Danon disease suggest that LAMP-2 may have distinct functions in the brain. Increased numbers of lipofuscin-like granules, corpora amylacea, Marinesco bodies and axonal spheroids at age of 31 may indicate accelerated senescence in the brain. Accumulations of electron-dense materials in neurons are consistent with the findings of lysosomal storage disease. Since a relationship between aging and lysosomal accumulation in the brain has

been discussed, the neuropathological findings in our case could be attributed to lysosomal dysfunction due to LAMP-2 deficiency.

The human LAMP-2 gene has nine exons and three splice-variants named LAMP-2A, LAMP-2B and LAMP-2C [5]. The exon-6-skipping mutation in our case causes molecular structural changes and may affect all three splice-variants including LAMP-2A, a receptor for CMA. However, one of the CMA substrates, α -synuclein, was not accumulated in our case. Recently, we found a novel function of LAMP-2C that was related to RNA degradation [3]. A patient with a mutation in exon 9b, which should affect only the LAMP-2B isoform, developed full symptoms including mental retardation (Nishino et al., patient 1) [6]. Further investigation regarding subtype-specific function is necessary to elucidate the mechanism of mental retardation.

References

1. Cuervo AM, Stefanis L, Fredenburg R et al (2004) Impaired degradation of mutant α -synuclein by chaperone-mediated autophagy. *Science* 305:1292–1295
2. Danon MJ, Oh SJ, DiMauro S et al (1981) Lysosomal glycogen storage disease with normal acid maltase. *Neurology* 31:51–57
3. Fujiwara Y, Furuta A, Kikuchi H et al Discovery of a novel type of autophagy targeting RNA. *Autophagy*. <http://dx.doi.org/10.4161/auto.23002>
4. Katsumi Y, Fukuyama H, Ogawa M et al (1996) Cerebral oxygen and glucose metabolism in glycogen storage disease with normal acid maltase: case report. *J Neurol Sci* 140:46–52
5. Konecki DS, Foetisch K, Zimmer KP et al (1995) An alternatively spliced form of the human lysosome-associated membrane protein-2 gene is expressed in a tissue-specific manner. *Biochem Biophys Res Commun* 215:757–767
6. Nishino I, Fu J, Tanji K et al (2000) Primary LAMP-2 deficiency causes X-linked vacuolar cardiomyopathy and myopathy (Danon disease). *Nature* 406:906–910